

LiftRefine: Progressively Refined View Synthesis from 3D Lifting with Volume-Triplane Representations

Tung Do¹, Thuan Hoang Nguyen¹, Anh Tuan Tran¹, Rang Nguyen¹, Binh-Son Hua^{1,2}

¹ VinAI Research, Vietnam

² Trinity College Dublin, Ireland

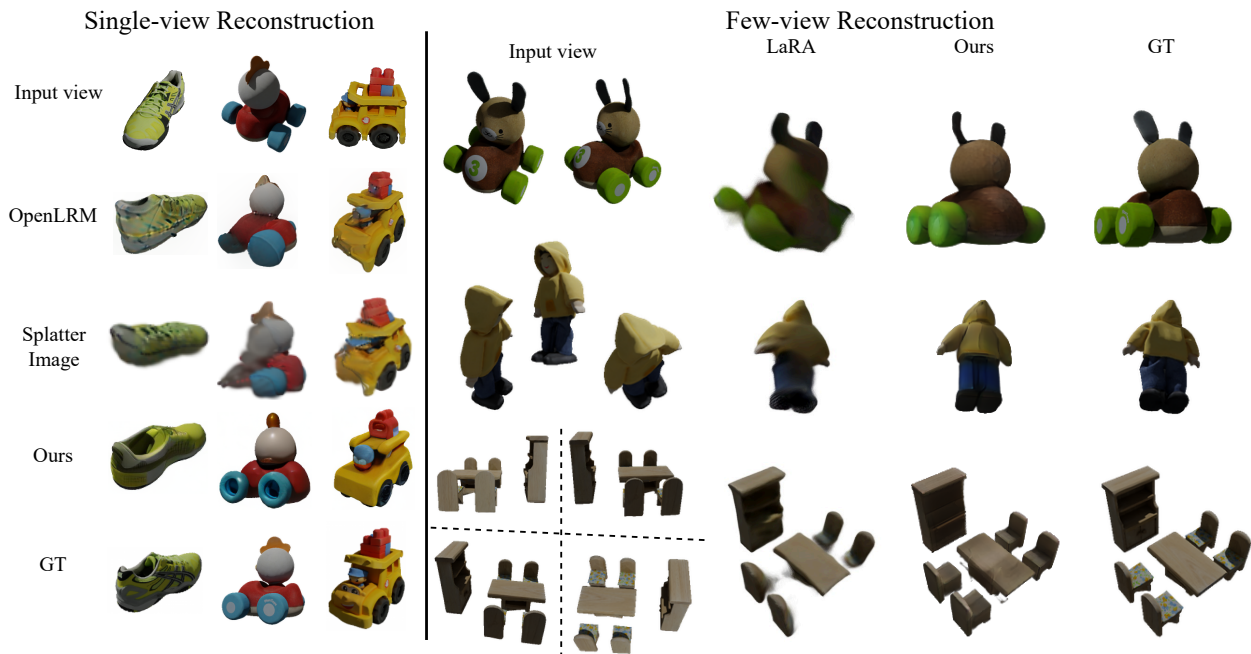


Figure 1: Our novel view synthesis addresses both single-view and few-view setting with high-quality reconstruction and rendering. Previous methods like OpenLRM (He and Wang 2023) and SplatterImage (Szymanowicz, Rupprecht, and Vedaldi 2023a) struggle to accurately reconstruct occluded regions, whereas our method can generate plausible results. For few-view reconstruction, LaRa (Chen et al. 2024) experiences a rapid decline in performance as the number of input views decreases. In contrast, our method consistently delivers faithful reconstructions across a wide range of input views.

Abstract

We propose a new view synthesis method via synthesizing a 3D neural field from both single or few-view input images. To address the ill-posed nature of the image-to-3D generation problem, we devise a two-stage method that involves a reconstruction model and a diffusion model for view synthesis. Our reconstruction model first lifts one or more input images to the 3D space from a volume as the coarse-scale 3D representation followed by a tri-plane as the fine-scale 3D representation. To mitigate the ambiguity in occluded regions, our diffusion model then hallucinates missing details in the rendered images from tri-planes. We then introduce a new progressive refine-

ment technique that iteratively applies the reconstruction and diffusion model to gradually synthesize novel views, boosting the overall quality of the 3D representations and their rendering. Empirical evaluation demonstrates the superiority of our method over state-of-the-art methods on the synthetic SRN-Car dataset, the in-the-wild CO3D dataset, and large-scale Objaverse dataset while achieving both sampling efficacy and multi-view consistency.

1 Introduction

View synthesis is a traditional task in computer vision and graphics with typical applications to enhance audience expe-

rience in entertainment and telepresence. At its core, view synthesis can be solved via image-based rendering and 3D reconstruction methods. The recent introduction of diffusion models (Ho, Jain, and Abbeel 2020) and neural radiance field (NeRF) (Mildenhall et al. 2020) have enabled high-quality image-based rendering and 3D reconstruction, renewing interest in effective and efficient view synthesis.

State-of-the-art view synthesis methods based on neural representations (Tucker and Snavely 2020; Yu et al. 2021; Wang et al. 2021; Chen et al. 2021; Mildenhall et al. 2020; Sitzmann, Zollhöfer, and Wetzstein 2019; Lin et al. 2023) tend to exhibit a mean-seeking behavior that often results in blurriness in unseen regions. Inspired by the advance of generative modeling, to address this limitation, several methods incorporate a generative model to synthesize details for the occluded regions. This approach can be tracked with two notable directions: image-based and 3D-based synthesis.

Particularly, image-based synthesis approach involves training an image diffusion model on the 2D view distribution. This method offers numerous advantages, such as directly leveraging prior knowledge from existing large pretrained diffusion models (e.g., Zero123 (Liu et al. 2023a) finetuned on Stable Diffusion (Rombach et al. 2021)). However, a notable challenge is that these methods cannot guarantee multi-view consistency among the generated images. Typically, they are coupled with auto-regressive sampling techniques or resort to test-time optimization (Poole et al. 2022; Wang et al. 2023), incurring a significant time cost.

In contrast to image-based models, 3D-based synthesis involves training a 3D diffusion model that ensures multi-view consistency as it directly predicts a 3D representation from the input views. However, training a 3D diffusion model requires substantial memory and the availability of 3D datasets remains limited in scale and diversity compared to massive 2D datasets such as LAION-5B (Schuhmann et al. 2022). These challenges hinder the scalability of this approach.

In this paper, we introduce a two-stage method that takes advantage of both 3D reconstruction and image synthesis for realistic novel view synthesis. In the first stage, we propose a novel reconstruction model that integrates both volume and tri-plane features. The motivation behind our fusion comes from two key considerations. Firstly, volumetric representation has demonstrated impressive results in various reconstruction models (Chan et al. 2023; Szymanowicz, Rupprecht, and Vedaldi 2023b; Karnewar et al. 2023), but its memory-intensive nature limits scalability. Conversely, tri-plane representation offers a more compact alternative that supports higher resolutions. However, existing approaches (Hong et al. 2024; Anciukevicius et al. 2022) face challenges in transforming 2D images into 3D tri-planes. Utilizing simplistic methods such as 2D-UNet or transformer-based architectures without geometry guidance often leads to mixed-up features within each tri-plane and an inability to capture high-frequency details of 3D objects. By combining volumetric and tri-plane representations, our approach effectively leverages the geometric interpretation provided by volumetric representation while enjoying the compactness of triplane representation. This integration enables us to overcome the limitations of each individual representation and enhance the

reconstruction capability of our model. In the second stage, our method focuses on the image-based diffusion paradigm, leveraging its efficiency and access to extensive literature and massive datasets. Inspired by Latent Diffusion (Rombach et al. 2021), our diffusion model operates in latent space to capture the distribution of novel views. More importantly, we devise a progressive inference procedure that iteratively applies both stages to gradually boost the quality of the 3D representation and rendered novel views across the initial and target view angles.

In summary, our contributions can be given as follows:

- We introduce a novel view synthesis method that employs a 3D reconstruction stage using both volumetric and tri-plane representations, along with an image synthesis stage based on image diffusion to predict novel views. We devise a training strategy to learn both the reconstruction model and the image diffusion model.
- We present a progressive inference procedure designed to systematically enhance the image quality of unseen regions by iteratively generating intermediate views from the input view toward the target view.
- We extensively conduct experiments on several datasets to validate our approach’s effectiveness, consistently showing substantial improvements over previous state-of-the-art methods, as shown in Fig.1.

2 Related work

Novel view synthesis has recently gained renewed attention thanks to the introduction of neural radiance fields (NeRFs) (Mildenhall et al. 2020). NeRF-based novel view synthesis is based on the concept of regressing a neural field from the input images (Tucker and Snavely 2020; Yu et al. 2021; Wang et al. 2021; Chen et al. 2021; Mildenhall et al. 2020; Sitzmann, Zollhöfer, and Wetzstein 2019; Lin et al. 2023) so that novel views at any camera pose can be rendered from this radiance field. A common issue of these methods is that when rendering occluded parts of the scene, these models tend to generate blurry images, primarily because they are mean estimators (Chan et al. 2023). A long series of work (Chan et al. 2023; Karnewar et al. 2023; Liu et al. 2023a; Tewari et al. 2023; Szymanowicz, Rupprecht, and Vedaldi 2023b; Chen et al. 2023; Rombach, Esser, and Ommer 2021; Ren and Wang 2022; Liu et al. 2021; Kim et al. 2023) focus on the use of generative models to capture the underlying distribution of the data in order to generate plausible content for unseen regions. For example, diffusion models (Liu et al. 2023a; Tseng et al. 2023; Zhou and Tulsiani 2023; Watson et al. 2022; Tewari et al. 2023; Szymanowicz, Rupprecht, and Vedaldi 2023b; Chen et al. 2023; Kim et al. 2023) have demonstrated the ability to synthesize realistic novel views when conditioned on an input image. (Kim et al. 2023) uses a two-stage design by first learning a 3D reconstruction model on a 2D dataset and then training a 3D diffusion model. (Chan et al. 2023; Zhou and Tulsiani 2023; Tseng et al. 2023) focus on a 3D-aware diffusion model to refine the deterministic 2D feature map into novel-view images. In the context of the diffusion-based novel view synthesis model, learning from

the 2D distribution of novel view images is favored over the 3D distribution of the dataset due to the use of massive pretrained 2D diffusion models and datasets.

2D Novel View Diffusion. Early research efforts (Chan et al. 2023; Gu et al. 2023; Tseng et al. 2023; Zhou and Tulsiani 2023; Watson et al. 2022) have been dedicated to capture the distribution of 3D objects by analyzing 2D novel image distributions. Notably, Tewari et al. (Tewari et al. 2023), despite only generating 2D images, have managed to synthesize outputs that closely mimic the 3D distribution, resulting in consistent and high-fidelity visuals. In a similar vein, GeNVS (Chan et al. 2023) leverages a volumetric representation of the input camera’s frustum to create a novel view feature map through volume rendering, which then is used as the condition for the diffusion model. Additionally, certain studies (Tseng et al. 2023; Zhou and Tulsiani 2023) employ epipolar lines to better guide the diffusion process. Whereas, another line of work (Watson et al. 2022; Liu et al. 2023a) omits explicit 3D geometrical modeling, relying solely on the capabilities of the diffusion model to generate novel 2D views. Despite these advancements, image-based diffusion models still encounter view inconsistency. To mitigate this issue, one ought to utilize auto-regressive sampling techniques to gradually generate the complete image sequences (Chan et al. 2023) or to employ test-time optimization with score distillation sampling (Gu et al. 2023; Zhou and Tulsiani 2023; Liu et al. 2023a), aiming for more accurate and consistent 3D representations.

3D Reconstruction Model. Multi-plane representation (Tucker and Snavely 2020) and the epipolar line constraint (Tseng et al. 2023; Zhou and Tulsiani 2023) are favored methods for novel-view synthesis due to their lightweight nature. However, these methods encounter difficulties when the target novel views are significantly different from the original input views. On the other hand, volumetric representation (Chan et al. 2023; Szymanowicz, Rupprecht, and Vedaldi 2023b; Karnewar et al. 2023) offers impressive accuracy without the above-mentioned limitation, although they suffers from a high memory footprint. To address such a problem, various methods (Hong et al. 2024; Anciukevicius et al. 2022; Chen et al. 2023) utilize a compact form of 3D volume called tri-plane. However, RenderDiffusion (Anciukevicius et al. 2022) adopts a 2D-UNet to encode 2D images and decode them into tri-planes, resulting in mixed-up features within the tri-plane due to the lack of geometry guidance. While LRM (Hong et al. 2024) demonstrates impressive performance on large-scale datasets, it still exhibits poor quality on smaller datasets such as SRN-Car.

In our work, LiftRefine leverages the synergy between a 3D fusion representation and 2D image diffusion to set new standards in novel view synthesis. By addressing the limitations of existing methods in handling 3D scenes, ensuring spatial consistency, and reconstructing fine details in occluded region, our work marks a significant advancement in 3D generation for both single-view and few-view settings.

3 Proposed Method

We take a two-stage approach for novel view synthesis. Stage 1 involves a reconstruction model that **lifts** input from a single view or few views to a neural 3D representation, and Stage 2 involves a diffusion model that **refines** the rendering from the neural representation by hallucinating details for occluded regions. The reconstruction model (Section 3.1) combines a volumetric radiance field and a tri-plane radiance field for both coarse- and fine-scale 3D representations. Like previous NeRF-based view synthesis methods (Mildenhall et al. 2020; Yu et al. 2021; Lin et al. 2023), our reconstruction model may produce blurry results in occluded regions due to the inherent ambiguity in unseen views. We propose a latent diffusion model conditioned on the novel view feature maps (Section 3.2) to refine view rendering. We propose progressive inference (Section 3.3) that exploits the view consistency of our reconstruction model and the hallucination ability of our diffusion model to effectively enhance the fidelity and completeness of the final reconstructed 3D scene.

3.1 Lift: 3D Reconstruction

In the first stage, our reconstruction model transforms the input view(s) into a 3D representation, utilizing both volumetric and tri-plane approaches to generate coarse- and fine-scale representation. An overview of our proposed reconstruction model is shown in Fig. 2.

Coarse-scale Volumetric Radiance Field. Given an input image $\mathcal{I}_{input} \in \mathbf{R}^{C \times H \times W}$ and its corresponding camera pose Ψ_{input} , we begin by extracting a feature map using a pretrained feature extractor (e.g., ResNet34, Dino-v2). Next, every voxel coordinate of a unit volume where the center is the world origin, is projected onto the image screen, and bilinear interpolation is applied to obtain the feature for each voxel. This process results in a coarse single-view volume feature. This coarse feature is then processed by a 3D convolutional encoder, the output of which is then aggregated via a cross-attention mechanism in the volume decoder to output a unified multi-view feature volume, similar to the approach in (Szymanowicz, Rupprecht, and Vedaldi 2023b). The final output of this stage is a coarse-scale multi-view feature volume $\mathcal{V}_{low} \in \mathbf{R}^{C \times D_c \times H_c \times W_c}$, where D_c, H_c, W_c are the coarse-scale volume dimension, respectively.

While the volumetric radiance field can be used to predict a 3D scene, the resulting images or features often suffer from low resolution, leading to visual artifacts such as blurriness and grid-like patterns. Although increasing the resolution of the feature volume could improve image quality, the memory requirements grow cubically $O(n^3)$ with the volume dimension n , quickly leading to out-of-memory issue. To address this problem, we gradually enhance the quality of the reconstructed images by progressively upsampling the low-resolution feature volume \mathcal{V}_{low} into high-resolution tri-plane \mathcal{T}_{high} . Leveraging tri-plane features allows us to achieve significantly higher resolution rendering compared to volumetric methods, thereby improving the quality of novel views.

Fine-scale Tri-plane Radiance Field. To reconstruct the tri-plane representation \mathcal{T}_{high} from a low-resolution feature volume \mathcal{V}_{low} , we first project the feature volume onto

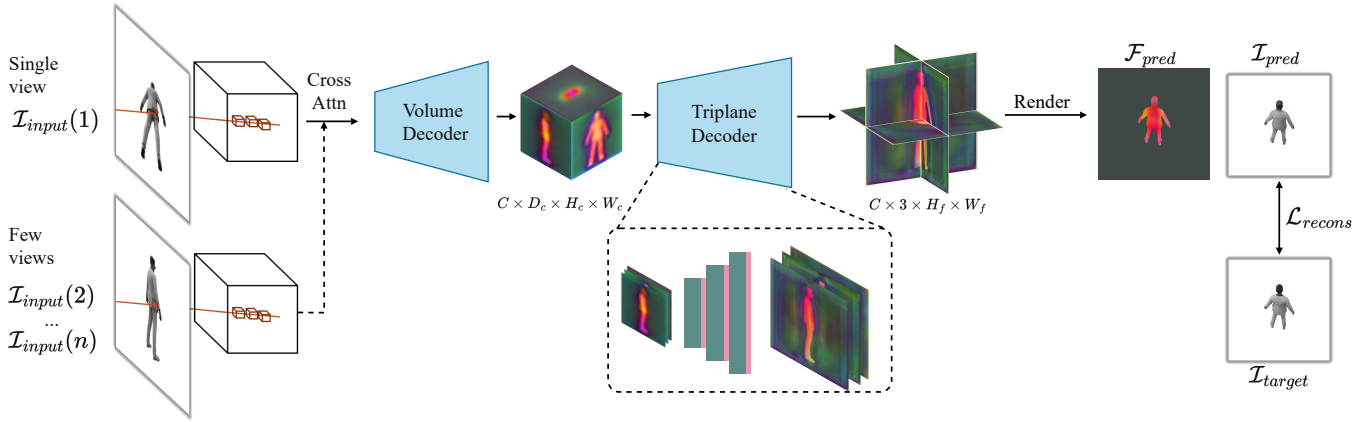


Figure 2: Our Stage 1 involves a reconstruction model to lift the input to 3D representations. Our model supports both single-view and few-view reconstruction, where all input features are aggregated into the volume decoder. The volume is then transformed into a triplane for rendering to novel view images and feature maps.

three orthogonal planes to form depth-aware feature planes F_{xy} , F_{xz} and F_{yz} . Each depth-aware feature plane is then fed to Triplane Decoder which consist of multiple upsampling blocks. Each block include a convolutional network with upsampling layers to refine details and increase the resolution. The final output of three feature planes is reshaped to construct the high-resolution tri-plane radiance field $\mathcal{T}_{high} \in \mathbf{R}^{C \times 3 \times H_f \times W_f}$, where H_f , W_f represent the fine-scale image dimensions. This tri-plane representation can then be rendered to generate color images and feature maps:

$$\mathcal{I}_{pred}, \mathcal{F}_{pred} = \mathcal{R}_{tri}(\mathcal{T}_{high}, \Psi_{target}), \quad (1)$$

where \mathcal{R}_{tri} is the function that renders the triplane to image \mathcal{I}_{pred} and feature map \mathcal{F}_{pred} at the target camera pose Ψ_{target} . The feature map \mathcal{F}_{pred} will be used as a condition for rendering diffusion in the following stage. To train the reconstruction model, we combine the standard L2 loss and LPIPS loss:

$$\mathcal{L}_{recons} = \|(\mathcal{I}_{pred} - \mathcal{I}_{target})\|_2^2 + \lambda \text{LPIPS}(\mathcal{I}_{pred}, \mathcal{I}_{target}). \quad (2)$$

We discover that our reconstructor excels at generating detailed 3D objects from just a few views. In fact, it performs well in rendering novel views with minimal ambiguity, even without the assistance of a diffusion model. However, when information on occluded regions is lacking, the reconstructor tends to produce blurry results. To overcome this issue, we incorporate a diffusion model, as detailed below.

3.2 Refine: Conditional Rendering Diffusion

In the second stage, our method refines blurry novel view images in the previous step using a diffusion model conditioned on the feature map rendered from the first stage. This second stage is depicted in Fig. 3. Our diffusion model, based on latent diffusion (Rombach et al. 2021), can be trained as follows. We first precompute a conditional rendering dataset, where each sample contains a pair of input view \mathcal{I}_{input} and

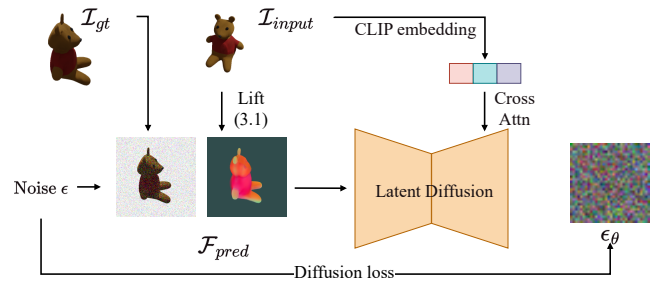


Figure 3: Our Stage 2 involves a conditional rendering diffusion model that aims to refine the rendered novel view from Stage 1 with additional details from a latent diffusion model.

a ground truth novel view \mathcal{I}_{gt} . We perform Stage 1 (Lift) to predict the feature map of the novel view \mathcal{F}_{pred} using Eq. 1. The denoising process of our latent diffusion model then follows. The key idea is to make the diffusion model learn to refine the novel view conditioned by the input view. Therefore, for each data sample and time step t , we add Gaussian noise $\epsilon \sim \mathcal{N}(0, I)$ to the novel view \mathcal{I}_{gt} , which is then concatenated with the predicted feature map \mathcal{F}_{pred} to form the input x_t for the denoising U-Net. We further extract the CLIP embedding of the input view \mathcal{I}_{input} and use this embedding to condition the U-Net via cross attentions. The diffusion model predicts the added noise, which is trained by the following diffusion loss:

$$\mathcal{L}_{diffusion} = \mathbb{E}_{t, \epsilon} \|\epsilon_{\theta}(x_t, t \mid \mathcal{F}_{pred}, \mathcal{I}_{clip}) - \epsilon\|_2^2, \quad (3)$$

where ϵ_{θ} is the denoising U-Net parameterized by θ .

3.3 Progressive Inference

In scenarios with significant ambiguities, the reconstruction model tends to produce blurry images in occluded regions, but albeit with strong view-to-view consistency. Conversely, the diffusion model generates high-quality results but may introduce inconsistencies across views. To leverage

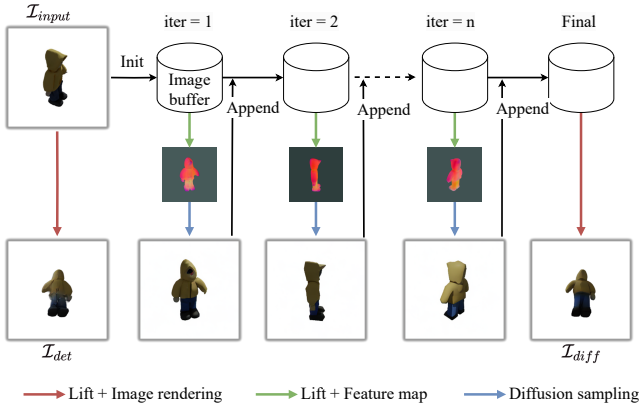


Figure 4: Progressive inference. Our method reconstructs and generates intermediated views, progressively refining the quality of the 3D representation and its rendering.

the strengths of both models, we introduce a progressive inference procedure that integrates the high-fidelity outputs from the diffusion model into the consistent 3D reconstructor, gradually filling in unseen regions and enhancing the overall reconstruction quality. This technique is demonstrated in Fig. 4.

Our inference process begins by initializing an image buffer to store all input views. In each iteration of the inference, we render a feature map using the reconstructor, conditioned on all images currently in the buffer. This feature map is then fed to the diffusion model, which generates an intermediate novel view image. The newly generated image is subsequently added to the buffer. All images in the buffer are then used for the next iteration to generate the next intermediate novel view image. At the final iteration, we applied the reconstructor to generate the final novel view image. In our experiments, for clarity, we refer to the novel views rendered by the reconstructor without using progressive inference as deterministic novel views \mathcal{I}_{det} , and novel views from progressive inference as \mathcal{I}_{diff} , respectively.

4 Experiments

Training. We first train our reconstruction model, followed by precomputing the conditional renderings to train the diffusion model. Our training is conducted on three different datasets: CO3D (Reizenstein et al. 2021), Objaverse (Deitke et al. 2022), and Shapenet-SRN Cars (Sitzmann, Zollhöfer, and Wetzstein 2019). The CO3D dataset, an in-the-wild collection, is utilized to assess the robustness of our method in real-world conditions where imperfections are present. The Objaverse dataset demonstrates the scalability of our model on a large-scale dataset. Finally, Shapenet-SRN Cars, a synthetic dataset focused on single-category objects, is employed in our ablation study. More details on ShapeNet-SRN Cars are provided in the supplementary material.

Inference. We evaluate our method with two different settings: deterministic and a diffusion-based. In the deterministic setting, we utilize the reconstruction model to synthesize

a tri-plane from the input view, and then render the novel view images *without* progressive refinement. In the diffusion-based setting, we employ progressive inference as outlined in Sec. 3.3, and use the final tri-plane to render the refined novel view. Please refer to supplementary material for video qualitative results.

Dataset and Evaluation Protocol. Some methods are trained for a specific setting, such as single-view or few-views reconstruction. Therefore, we divide our evaluation protocol into these two settings. Notably, our method is effective in both scenarios.

We conduct both single-view and few-views evaluations on the CO3D dataset (Reizenstein et al. 2021) and the Google Scanned Object (GSO) dataset (Francis et al. 2022). We assess our method at a resolution of 128x128 for in-the-wild CO3D dataset (Reizenstein et al. 2021) and 256x256 for the GSO dataset (Francis et al. 2022).

4.1 CO3D

On the CO3D dataset, we conduct a comparative analysis on four classes (Hydrant, Teddybear, Vase and Plant) on two state-of-the-art methods: ViewsetDiffusion (Szymanowicz, Rupprecht, and Vedaldi 2023b) and SparseFusion (Zhou and Tulsiani 2023). The quantitative results are summarized in Tab. 1. In both single-view and few-views reconstruction tasks, our model consistently surpasses previous methods across key metrics, including PSNR, SSIM, and LPIPS, highlighting its effectiveness in capturing fine details and preserving image quality. In the diffusion setting, while there is a decrease in pixel-wise metrics, our approach shows improvements in object quality, evidenced by better SSIM and LPIPS scores. Additionally, for the distribution-based metric FID, our diffusion-based setting demonstrates significant gains over the deterministic setting, indicating the efficacy of progressive inference in enhancing the overall quality of the generated images. It is important to note that SparseFusion generates images, while ViewsetDiffusion and our method reconstruct 3D representations. Consequently, SparseFusion exhibits a higher FID but lower consistency compared to our method.

In Fig. 5, for a deterministic setting with a single input view, we observe high-quality synthesis in visible regions but encounter blurriness in occluded areas. Upon employing progressive inference, the final object fidelity is significantly improved, approaching the performance achieved in the deterministic setting with three input views. For results on multi-view consistency, please refer to the supplementary material, where a video presentation is provided.

4.2 Google Scanned Object

On the GSO dataset, we compare our method under the single-view setting with OpenLRM (He and Wang 2023), an open-source version of the LRM model (Hong et al. 2024), and Splatter Image (Szymanowicz, Rupprecht, and Vedaldi 2023a), as these methods are designed for single-view reconstruction. Results are shown in Tab. 2 and Fig. 1. Our model outperforms previous methods for more than 1 db in PSNR while having competitive performance on SSIM and LPIPS.

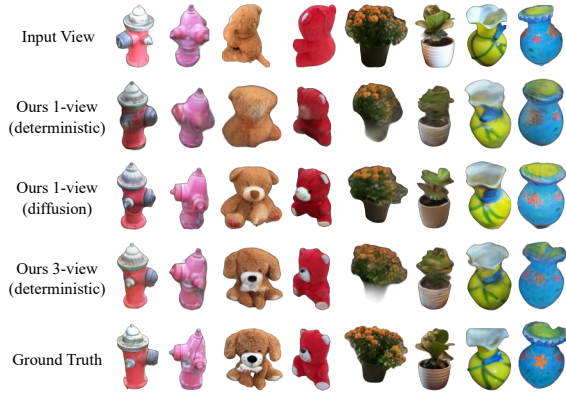


Figure 5: Qualitative results on CO3D Dataset.

	1-view			
	PSNR \uparrow	SSIM \uparrow	LPIPS \downarrow	FID \downarrow
SparseFusion	16.45	0.652	0.278	46.5
ViewsetDiffusion	18.41	0.684	0.280	99.6
Ours (Det)	20.38	0.747	<u>0.204</u>	73.4
Ours (Diff)	<u>20.10</u>	<u>0.744</u>	0.195	39.6
	3-view			
	PSNR \uparrow	SSIM \uparrow	LPIPS \downarrow	FID \downarrow
SparseFusion	21.48	0.773	0.175	29.3
ViewsetDiffusion	21.86	0.752	0.241	91.7
Ours (Det)	22.82	0.800	<u>0.166</u>	59.5
Ours (Diff)	<u>22.66</u>	<u>0.797</u>	0.161	<u>43.3</u>

Table 1: Results on CO3D dataset for single and few-view reconstruction.

Compared to LRM which is purely transformer-based, our method effectively leverages inductive bias from the volume and triplane representations, leading to more robust models with reduced training time. Our method requires 4 NVIDIA A100 GPUs for training in 7 days while LRM needs 128 A100 GPUs for training in 3 days.

In the few-view reconstruction task, we compare our model with the current SOTA method LaRa (Chen et al. 2024). The results is shown in Tab. 2. Our model outperforms LaRa significantly when using 2 or 3 input views and remains competitive with 4 input views. This advantage arises from our volume-based representation, which excels at reconstructing unseen regions. In contrast, LaRa’s Gaussian splatting method struggles to render occluded areas when input views are limited.

4.3 Ablation Study

In this section, we validate the impact of our design choices. Unless otherwise mentioned, we drop the 2D conditional diffusion model and perform the ablation studies with the deterministic setting.

Analysis of 3D Representations. To demonstrate the efficacy

# Views	Method	PSNR \uparrow	SSIM \uparrow	LPIPS \downarrow
1	OpenLRM	18.06	0.840	0.129
	Splatter Image	21.06	0.880	0.111
	Ours (Det)	22.23	0.880	0.113
	Ours (Diff)	22.55	0.895	0.116
2	LaRa	19.59	0.877	0.151
	Ours (Det)	23.82	0.908	0.092
	Ours (Diff)	23.91	0.909	0.090
3	LaRa	23.92	0.915	0.112
	Ours (Det)	24.99	0.916	0.085
	Ours (Diff)	25.11	0.917	0.083
4	LaRa	26.03	0.930	0.098
	Ours (Det)	25.64	0.920	0.082
	Ours (Diff)	25.79	0.922	0.080

Table 2: Results on GSO dataset for single and few-view reconstruction.

Method	PSNR \uparrow	SSIM \uparrow	LPIPS \downarrow
Default	24.56	0.868	0.100
B	24.06	0.860	0.113
C	23.66	0.853	0.111

Table 3: Experiments with the impact of three different configurations for the 3D reconstructor on CO3D dataset

of incorporating low-resolution volume and high-resolution tri-plane representations, we conducted several experiments on CO3D-Hydrant, as shown in Tab. 3. Our method is denoted as the default setting. Firstly, by replacing our upsampler layers with bicubic interpolation (setting C), we observed a significant drop in the performance of the reconstructor, nearly 1dB. This indicates the importance of our upsampler in preserving image quality and details during reconstruction. Additionally, we replaced the low-resolution volume features with low-resolution tri-plane representations (setting B). We achieved this by projecting the volume features, obtained after lifting from the input view, onto a tri-plane, and then replacing every 3D layer in the 3D encoder and decoder with 2D convolutional layers to operate on tri-plane features. However, the results showed that the performance of setting B is inferior to using volume features as the low-resolution representation. We hypothesize that this is because working on volume at low-resolution allows for more informative 3D features rather than its compact tri-plane version.

Analysis of Image-to-Triplane Backbone. To study the importance of the low-resolution volume, we conducted a series of experiments with different image-to-triplane backbones. The quantitative results are presented in Tab. 4. Firstly, we utilized LRM (Hong et al. 2024), a transformer-based reconstruction model renowned for its ability to output tri-plane representations from single images. While LRM demonstrated remarkable performance when applied to large datasets, its efficacy diminishes when working on smaller datasets such as ShapeNet-SRN Cars. This is because the

Method	PSNR \uparrow	SSIM \uparrow	LPIPS \downarrow
OpenLRM	22.88	0.910	0.082
Triplane	21.83	0.898	0.087
Volume	22.78	0.908	0.087
Ours	23.76	0.921	0.067

Table 4: Quantitative results with different image-to-triplane architecture on ShapeNet-SRN Cars dataset.

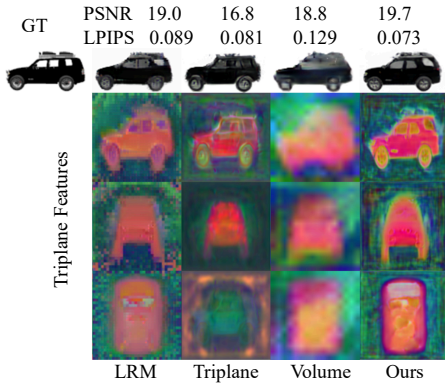


Figure 6: Feature maps of a ShapeNet-SRN Car example with different image-to-triplane backbones.

transformers are unaware of 3D inductive bias, and instead are tasked to implicitly learn spatial relationship, which deteriorates its performance when training on a small dataset like ShapeNet. Notably in Fig. 6, the tri-plane features from LRM exhibited pixelated noise, thereby impairing its overall performance. Subsequently, following (Anciukevicius et al. 2022), we leveraged a 2D UNet to encode and decode 2D images into 3D tri-planes without volume representation. However, we encountered a significant challenge as the output tri-plane appears mixed up due to the absence of channel decoupling during the encoding and decoding stages of the 2D UNet. Consequently, this led to a notable drop in the PSNR metric, indicating a degradation in the quality of reconstruction. Lastly, we modify our backbone to use only the volume representation. The results were blurry due to the low volume resolution, resulting in high PSNR but low LPIPS scores.

Study on Progressive Inference. We investigated the effects of increasing the number of iterations during progressive inference. In Tab. 5, while we observed a decline in pixel-wise metrics such as PSNR and SSIM, there was a clear improvement in the semantic quality of the generated images, reflected by metrics like FID. We found that using 4 iterations leads to the best balanced result across metrics. Therefore, we used 4 iterations for progressive refinement in our experiments.

Comparison with Multi-view Generation. To position our method against SOTA methods in multi-view generation (Shi et al. 2024; Wang and Shi 2023; Long et al. 2024; Liu et al. 2023b; Xu et al. 2024), we compare our method with SyncDreamer (Liu et al. 2023b), a multi-view diffusion model

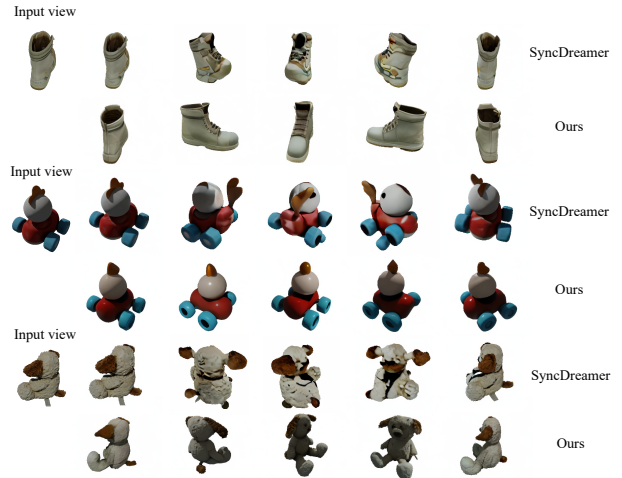


Figure 7: Qualitative comparison with SyncDreamer.

# iters	PSNR \uparrow	SSIM \downarrow	LPIPS \downarrow	FID \downarrow
0	22.64	0.834	0.118	42.7
1	22.61	0.845	0.105	37.0
2	22.43	0.843	0.107	35.4
4	22.12	0.840	0.108	34.7
6	21.89	0.836	0.111	34.0
8	21.73	0.834	0.113	34.7

Table 5: The impact of the number of interpolated views on the single-view reconstruction task with CO3D-Hydrant.

that generates 16 views from input images. We found that although SyncDreamer demonstrates impressive view consistency, their method only works well for input views at frontal angles. Their performance significantly deteriorates when synthesizing from side or rear views of objects. In contrast, our method consistently maintains high-fidelity images across all perspectives as shown in Fig. 7. For a quantitative comparison with SyncDreamer on novel view synthesis, please refer to the supplementary material.

5 Discussion and Conclusion

In conclusion, this paper introduces LiftRefine, a new method for novel view synthesis combining 3D reconstruction with image-based diffusion empowered by a progressive refinement procedure. Our two-stage method achieves SOTA results, delivering realistic and consistent novel views. Extensive testing on diverse datasets validates its effectiveness.

While our method produces plausible results across datasets, we found that our method struggles in some cases such as the Plant category in CO3D, where the synthesized novel views tend to be blurry. This could be because of the high-resolution details in the plant images that are not well captured by the current resolution of our representations. Improving the high-frequency rendering of this category would be our future work.

References

- Anciukevicius, T.; Xu, Z.; Fisher, M.; Henderson, P.; Bilen, H.; Mitra, N. J.; and Guerrero, P. 2022. RenderDiffusion: Image Diffusion for 3D Reconstruction, Inpainting and Generation. *arXiv*.
- Chan, E. R.; Nagano, K.; Chan, M. A.; Bergman, A. W.; Park, J. J.; Levy, A.; Aittala, M.; Mello, S. D.; Karras, T.; and Wetzstein, G. 2023. GeNVS: Generative Novel View Synthesis with 3D-Aware Diffusion Models. In *arXiv*.
- Chen, A.; Xu, H.; Esposito, S.; Tang, S.; and Geiger, A. 2024. LaRa: Efficient Large-Baseline Radiance Fields. In *European Conference on Computer Vision (ECCV)*.
- Chen, A.; Xu, Z.; Zhao, F.; Zhang, X.; Xiang, F.; Yu, J.; and Su, H. 2021. Mvsnerf: Fast generalizable radiance field reconstruction from multi-view stereo. In *ICCV*.
- Chen, H.; Gu, J.; Chen, A.; Tian, W.; Tu, Z.; Liu, L.; and Su, H. 2023. Single-Stage Diffusion NeRF: A Unified Approach to 3D Generation and Reconstruction. In *ICCV*.
- Deitke, M.; Schwenk, D.; Salvador, J.; Weihs, L.; Michel, O.; VanderBilt, E.; Schmidt, L.; Ehsani, K.; Kembhavi, A.; and Farhadi, A. 2022. Objaverse: A Universe of Annotated 3D Objects. *arXiv preprint arXiv:2212.08051*.
- Francis, A. G.; Kinman, B.; Reymann, K. A.; Downs, L.; Koenig, N.; Hickman, R. M.; McHugh, T. B.; and Vanhoucke, V. O., eds. 2022. *Google Scanned Objects: A High-Quality Dataset of 3D Scanned Household Items*.
- Gu, J.; Trevithick, A.; Lin, K.-E.; Susskind, J.; Theobalt, C.; Liu, L.; and Ramamoorthi, R. 2023. NerfDiff: Single-image View Synthesis with NeRF-guided Distillation from 3D-aware Diffusion. In *ICML*.
- He, K.; Zhang, X.; Ren, S.; and Sun, J. 2016. Deep Residual Learning for Image Recognition. *CVPR*.
- He, Z.; and Wang, T. 2023. OpenLRM: Open-Source Large Reconstruction Models. <https://github.com/3DTopia/OpenLRM>.
- Ho, J.; Jain, A.; and Abbeel, P. 2020. Denoising Diffusion Probabilistic Models. *CVPR*.
- Hong, Y.; Zhang, K.; Gu, J.; Bi, S.; Zhou, Y.; Liu, D.; Liu, F.; Sunkavalli, K.; Bui, T.; and Tan, H. 2024. LRM: Large Reconstruction Model for Single Image to 3D.
- Karnewar, A.; Vedaldi, A.; Novotny, D.; and Mitra, N. 2023. HoloDiffusion: Training a 3D Diffusion Model using 2D Images. In *CVPR*.
- Kim, S. W.; Brown, B.; Yin, K.; Kreis, K.; Schwarz, K.; Li, D.; Rombach, R.; Torralba, A.; and Fidler, S. 2023. NeuralField-LDM: Scene Generation with Hierarchical Latent Diffusion Models. In *CVPR*.
- Kingma, D. P.; and Ba, J. 2017. Adam: A Method for Stochastic Optimization. *arXiv:1412.6980*.
- Lin, K.-E.; Yen-Chen, L.; Lai, W.-S.; Lin, T.-Y.; Shih, Y.-C.; and Ramamoorthi, R. 2023. Vision Transformer for NeRF-Based View Synthesis from a Single Input Image. In *WACV*.
- Liu, A.; Tucker, R.; Jampani, V.; Makadia, A.; Snavely, N.; and Kanazawa, A. 2021. Infinite Nature: Perpetual View Generation of Natural Scenes from a Single Image. In *ICCV*.
- Liu, R.; Wu, R.; Hoorick, B. V.; Tokmakov, P.; Zakharov, S.; and Vondrick, C. 2023a. Zero-1-to-3: Zero-shot One Image to 3D Object. *arXiv:2303.11328*.
- Liu, Y.; Lin, C.; Zeng, Z.; Long, X.; Liu, L.; Komura, T.; and Wang, W. 2023b. SyncDreamer: Learning to Generate Multiview-consistent Images from a Single-view Image. *arXiv preprint arXiv:2309.03453*.
- Long, X.; Guo, Y.-C.; Lin, C.; Liu, Y.; Dou, Z.; Liu, L.; Ma, Y.; Zhang, S.-H.; Habermann, M.; Theobalt, C.; et al. 2024. Wonder3D: Single Image to 3D using Cross-Domain Diffusion. In *CVPR*.
- Mildenhall, B.; Srinivasan, P. P.; Tancik, M.; Barron, J. T.; Ramamoorthi, R.; and Ng, R. 2020. NeRF: Representing Scenes as Neural Radiance Fields for View Synthesis. In *ECCV*.
- Poole, B.; Jain, A.; Barron, J. T.; and Mildenhall, B. 2022. DreamFusion: Text-to-3D using 2D Diffusion. *arXiv*.
- Reizenstein, J.; Shapovalov, R.; Henzler, P.; Sbordone, L.; Labatut, P.; and Novotny, D. 2021. Common Objects in 3D: Large-Scale Learning and Evaluation of Real-life 3D Category Reconstruction. In *ICCV*.
- Ren, X.; and Wang, X. 2022. Look Outside the Room: Synthesizing A Consistent Long-Term 3D Scene Video from A Single Image. In *CVPR*.
- Rombach, R.; Blattmann, A.; Lorenz, D.; Esser, P.; and Ommer, B. 2021. High-Resolution Image Synthesis with Latent Diffusion Models. *arXiv:2112.10752*.
- Rombach, R.; Esser, P.; and Ommer, B. 2021. Geometry-Free View Synthesis: Transformers and no 3D Priors. *arXiv:2104.07652*.
- Schuhmann, C.; Beaumont, R.; Vencu, R.; Gordon, C.; Wightman, R.; Cherti, M.; Coombes, T.; Katta, A.; Mullis, C.; Wortsman, M.; Schramowski, P.; Kundurthy, S.; Crowson, K.; Schmidt, L.; Kaczmarczyk, R.; and Jitsev, J. 2022. LAION-5B: An open large-scale dataset for training next generation image-text models. *arXiv:2210.08402*.
- Shi, Y.; Wang, P.; Ye, J.; Mai, L.; Li, K.; and Yang, X. 2024. MVDream: Multi-view Diffusion for 3D Generation. In *ICLR*.
- Sitzmann, V.; Zollhöfer, M.; and Wetzstein, G. 2019. Scene Representation Networks: Continuous 3D-Structure-Aware Neural Scene Representations. In *NeurIPS*.
- Song, J.; Meng, C.; and Ermon, S. 2022. Denoising Diffusion Implicit Models. *arXiv:2010.02502*.
- Szymanowicz, S.; Rupprecht, C.; and Vedaldi, A. 2023a. Splatter Image: Ultra-Fast Single-View 3D Reconstruction. In *arXiv*.
- Szymanowicz, S.; Rupprecht, C.; and Vedaldi, A. 2023b. Viewset Diffusion: (0-)Image-Conditioned 3D Generative Models from 2D data. In *ICCV*.
- Tewari, A.; Yin, T.; Cazenavette, G.; Rezchikov, S.; Tenenbaum, J. B.; Durand, F.; Freeman, W. T.; and Sitzmann, V. 2023. Diffusion with Forward Models: Solving Stochastic Inverse Problems Without Direct Supervision. In *arXiv*.

Tseng, H.-Y.; Li, Q.; Kim, C.; Alsisan, S.; Huang, J.-B.; and Kopf, J. 2023. Consistent View Synthesis with Pose-Guided Diffusion Models. In *CVPR*.

Tucker, R.; and Snavely, N. 2020. Single-view View Synthesis with Multiplane Images. In *CVPR*.

Wang, P.; and Shi, Y. 2023. ImageDream: Image-Prompt Multi-view Diffusion for 3D Generation. *arXiv preprint arXiv:2312.02201*.

Wang, Q.; Wang, Z.; Genova, K.; Srinivasan, P.; Zhou, H.; Barron, J. T.; Martin-Brualla, R.; Snavely, N.; and Funkhouser, T. 2021. IBRNet: Learning Multi-View Image-Based Rendering. In *CVPR*.

Wang, Z.; Lu, C.; Wang, Y.; Bao, F.; Li, C.; Su, H.; and Zhu, J. 2023. ProlificDreamer: High-Fidelity and Diverse Text-to-3D Generation with Variational Score Distillation. *arXiv preprint arXiv:2305.16213*.

Watson, D.; Chan, W.; Martin-Brualla, R.; Ho, J.; Tagliasacchi, A.; and Norouzi, M. 2022. Novel View Synthesis with Diffusion Models. *arXiv:2210.04628*.

Xu, Y.; Tan, H.; Luan, F.; Bi, S.; Wang, P.; Li, J.; Shi, Z.; Sunkavalli, K.; Wetzstein, G.; Xu, Z.; and Zhang, K. 2024. DMV3D: Denoising Multi-View Diffusion using 3D Large Reconstruction Model. In *ICLR*.

Yu, A.; Ye, V.; Tancik, M.; and Kanazawa, A. 2021. pixel-NeRF: Neural Radiance Fields from One or Few Images. In *CVPR*.

Zhou, Z.; and Tulsiani, S. 2023. SparseFusion: Distilling View-conditioned Diffusion for 3D Reconstruction. In *CVPR*.

LiftRefine: Progressively Refined View Synthesis from 3D Lifting with Volume-Triplane Representations

Supplementary Material

Abstract

In this supplementary document, we first provide more details about our architecture design in Sec. 6, and then discuss training and inference details in Sec. 7. We then present additional experiments in Sec. 8 with more qualitative results in Sec. 9. Readers are encouraged to view the supplementary videos for more visual results of our method.

6 Architecture

6.1 Reconstructor

Our reconstructor takes in N input frames and outputs a single feature tri-plane representation that can be used to render arbitrary novel views.

Encoder. Our encoder is based on ViewsetDiffusion (Szymanowicz, Rupprecht, and Vedaldi 2023b) but we replace the feature extractor with a pretrained ResNet34 (He et al. 2016) or Dino-V2 for enhanced feature extraction capabilities. We adjust the output of the reconstructor, changing from a radiance field volume to a feature volume by increasing the channel dimension from 4 to 32.

Decoder. Our tri-plane decoder architecture is based on a 2D UNet decoder (Ho, Jain, and Abbeel 2020), comprising multiple upsampler blocks. Each upsampler block consists of a ResNet block, an upsample layer, and a self-attention layer at the end. Further details on our tri-plane decoder are illustrated in Fig. 8. In our experiments, we upscale the resolution of the feature volume, initially sized at 32, to a feature tri-plane with resolution of 256.

6.2 Diffusion model

Our diffusion operates in the latent space, where we use a VAE model to map an input image $\mathcal{I} \in \mathbb{R}^{3 \times 256 \times 256}$ to a latent representation $z \in \mathbb{R}^{4 \times 32 \times 32}$. We use the UNet architecture from Zero123 (Liu et al. 2023a) for our 2D conditional diffusion model and increase the condition channel of the original Zero123 model from 4 to 32 to match our conditional feature map. Additionally, we leverage their pretrained model as an initialization for our training process.

7 Implementation Details

Training. In the first stage, we train the reconstructor until the validation accuracy stall. For data sampling strategy, we randomly sample 1 to 3 image(s) as input \mathcal{I}_{input} and 1 image as \mathcal{I}_{target} . After that, we precompute the conditional renderings and follow the same data sampling strategy as training reconstructor to train the diffusion model.

Inference. We use progressive inference (Fig. 4 in our main paper) to combine our 3D reconstructor and our 2D diffusion model. For CO3D dataset, we interpolate n camera poses between the input and target camera pose. For GSO dataset,

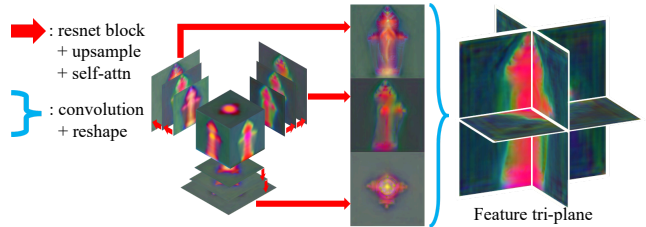


Figure 8: The tri-plane decoder architecture takes a feature volume as input. This feature is then projected into three orthogonal planes to form depth-aware feature planes. Each of these feature planes undergoes processing through multiple upsampler blocks, illustrated by the red arrows. Finally, the feature planes are passed through a final convolution layer and reshaped (depicted by a blue bracket) to form a feature tri-plane.

we calculate the azimuth and elevation of input view and interpolate n camera poses on the spherical trajectory. In our main experiment, we employ 200-steps DDIM sampling (Song, Meng, and Ermon 2022) with classifier free guidance = 2.0 to sample the images.

Optimization. We employ the Adam optimizer (Kingma and Ba 2017) and cosine scheduler with a learning rate of 1×10^{-6} for our reconstructor and 1×10^{-7} for our diffusion model. We set the maximum 300k training steps and but stop the training if there is no improvement. The total batch size is 128 and 256 across 4 A100 GPUs for reconstructor and diffusion model respectively. In \mathcal{L}_{recons} , we set λ to 0.1 for all experiments.

8 Additional Experiments

Results on ShapeNet-SRN Cars. We evaluate our method at a resolution of 128x128 for the single-view reconstruction on ShapeNet-SRN Cars dataset (Sitzmann, Zollhöfer, and Wetzstein 2019). Following the evaluation protocol from PixelNeRF (Yu et al. 2021), we adopt their train/val/test split and utilize the 64th view as input, while the remaining 250 views serve as unseen target views. For Shapenet SRN-Car, we employ the pretrained models from the baselines for inference whenever available. Otherwise, we utilize their reported results for our quantitative analysis.

In Tab. 6, we provide a comprehensive evaluation of our method in comparison to SOTA methods. In the deterministic setting, our model demonstrates superior quantitative performance, notably surpassing regression-based models such as PixelNeRF (Yu et al. 2021) and VisionNeRF (Lin et al. 2023) across pixel-wise metrics like PSNR and SSIM, as well as perceptual metric LPIPS. Additionally, our approach outperforms probabilistic-based methods such as GeNVS (Chan et al. 2023) and ViewSet Diffusion (Szymanowicz,



Figure 9: Novel view synthesis from a single input image on CO3D dataset.

Method	PSNR \uparrow	SSIM \uparrow	LPIPS \downarrow	FID \downarrow
PixelNerf	23.17	0.90	0.111	64.08
VisionNerf	22.87	0.90	0.084	24.24
SSDNeRF	23.52	0.91	0.078	16.39
GeNVS	20.07	0.89	0.104	6.47
Viewset Diffusion	23.29	0.91	0.094	39.54
Splatter Image	24.00	0.92	0.078	-
Ours (deterministic)	24.20	0.92	0.057	6.44
Ours (diffusion)	23.67	0.92	0.061	6.08

Table 6: Single-view novel view synthesis on ShapeNet-SRN Cars (Sitzmann, Zollhöfer, and Wetzstein 2019).

Rupprecht, and Vedaldi 2023b) in FID. Our deterministic setting generates plausible output in occluded regions, whereas ViewsetDiffusion with diffusion still yields blurry results or hallucinates implausible outcomes. For instance, the trunk of the car appears blurry and grey instead of maintaining a similar color to the front, as illustrated in Fig. 10.

In the diffusion setting, with the incorporation of progressive inference, our model achieves even better results in distribution-based metrics (FID). However, it is worth noting that there is a slight decrease in pixel-wise metrics, namely PSNR and SSIM, due to the fact that these metrics are more favorable for mean-seeking models, as discussed in (Chan et al. 2023). The incorporation of a 2D diffusion model significantly reduces blurriness in the final output of the generative setting. Notably, the output of the car remains interpretable, even when considering only the input view (the last two columns in Fig. 10).

Study on Tri-plane Resolution. We investigate the impact of varying tri-plane resolution on reconstruction quality. We start from volumetric representation (volume dimensions equal to 16^3) and then add a tri-plane decoder which gradu-

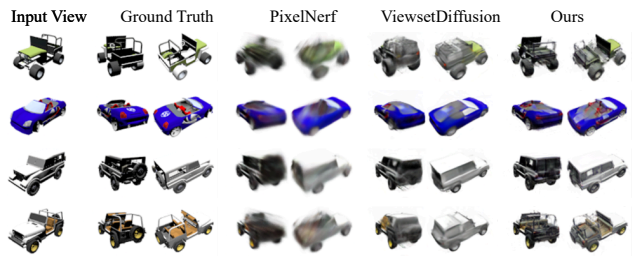


Figure 10: Qualitative results on SRN-Cars.

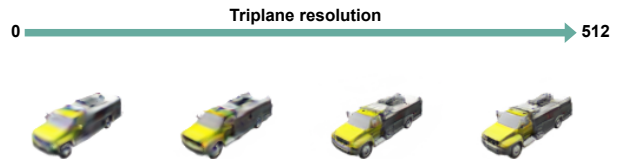


Figure 11: The effect of coarse and fine resolution of the 3D representations on final image quality (volume resolution - triplane resolution).

ally increases the tri-plane resolution. The results in Tab. 7 demonstrate a clear trend: as the tri-plane resolution increases, the quality of novel view images improves noticeably. As shown in Fig. 11, the rendered images indicate enhanced sharpness as the tri-plane resolution grows higher.

9 Qualitative Results

Qualitative results on Shapenet SRN-Car. We present additional qualitative results on Shapenet SRN-Car in Table 13. While our deterministic setting achieves good quality in the reconstruction view, it tends to produce blurry results in high ambiguity regions, like the back of the car. However, after progressive inference, our diffusion setting generates a plausible result with significantly reduced blurriness.

We include small and non-centric samples for Shapenet SRN-Car in Fig. 12. Despite ViewsetDiffusion (Szymanow-

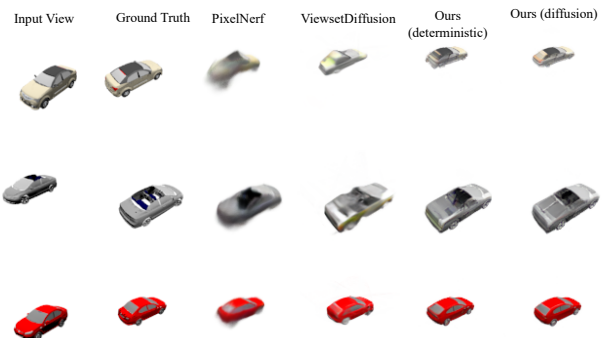


Figure 12: Qualitative results of small, non-centric sample on Shapenet SRN-Cars.

Triplane resolution	PSNR \uparrow	SSIM \uparrow	LPIPS \downarrow
None	22.78	0.908	0.087
16	23.07	0.912	0.081
32	23.53	0.918	0.069
64	23.70	0.920	0.078
128	23.76	0.921	0.067
256	23.79	0.92	0.066

Table 7: Experiments on different triplane resolution with SRN-Car dataset.

icz, Rupprecht, and Vedaldi 2023b) being a probabilistic model, it still generates blurry results and saturated colors, as seen in the first row. PixelNerf (Yu et al. 2021) and our deterministic setting are regressive models, yet our method produces significantly improved results. Moreover, with progressive inference, our diffusion setting generates realistic, sharper outcomes in all samples.

Qualitative results on CO3D. We present additional qualitative results for each category of the CO3D dataset in Fig. 9, with Hydrant in Fig. 15, Teddybear in Fig. 16, Vase in Fig. 17, and Plant in Fig. 18. Our deterministic setting can reconstruct with mild ambiguity but tends to be blurry in high ambiguity regions, while our diffusion setting has the capability to hallucinate the unseen regions with plausible results.

While our method produces plausible results for most categories in CO3D, we found that examples in the Plant category are the most challenging, where the synthesized novel views tend to be blurry. This could be because of the high-frequency details in the plant images that are not well captured by the current resolution of our representations. Improving the high-frequency rendering of this category would be future work.

Diversity of generated images. We demonstrate the diversity of the diffusion model by sampling a novel view multiple times on CO3D dataset. As shown in Fig. 14, each sample exhibits a distinct appearance while being consistent with the input view.

Qualitative results on GSO. We provide additional qualitative results for single-view and two-view reconstructions in Fig.19 and Fig.20. The images generated by the diffusion model, shown in the Fig.21, exhibit minor inconsistencies across views, but their fidelity is significantly higher compared to the renderings produced by our 3D representation.

Comparison with SyncDreamer on GSO dataset. We compare our deterministic model with the multi-view diffusion method, SyncDreamer (Liu et al. 2023b), in Table 8. While our approach demonstrates competitive performance against SyncDreamer, it also offers greater flexibility. Unlike SyncDreamer, which generates only 16 views at a fixed elevation of 0 degrees, our method can accept arbitrary input view(s) and render at any desired pose(s).

Method	PSNR \uparrow	SSIM \uparrow	LPIPS \downarrow
SyncDreamer	19.46	0.83	0.142
Ours	19.49	0.82	0.180

Table 8: Comparison with SyncDreamer on GSO dataset. While SyncDreamer produces perceptually better results, it can only generate a fixed set of 16 views at fixed camera angles from a frontal input view. By contrast, our method can generate novel views with input/output at arbitrary camera angles.

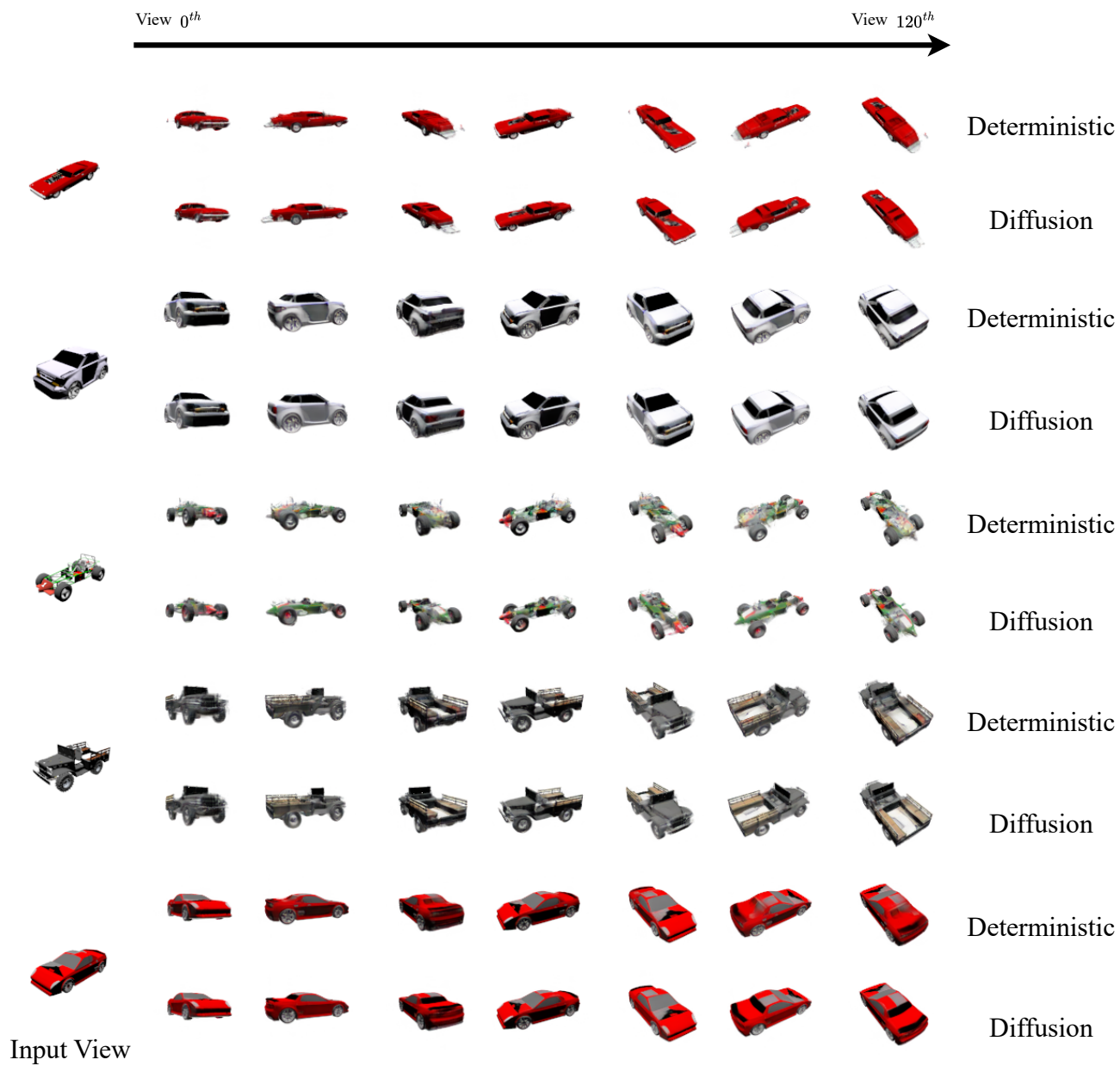


Figure 13: Qualitative results on Shapenet SRN-Cars.

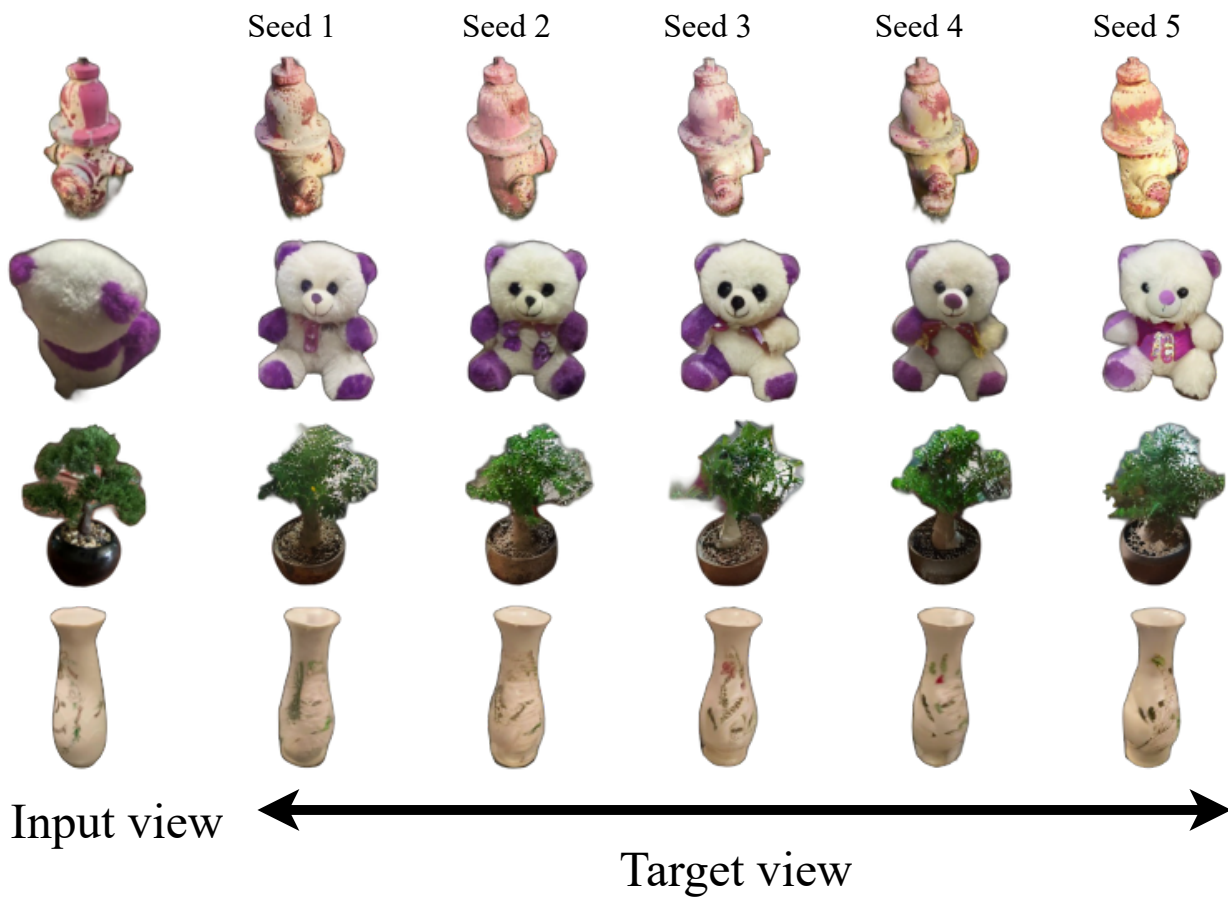


Figure 14: Sample diversity on CO3D dataset. Our diffusion model generates various feasible target views, all of which are consistent with the input view.

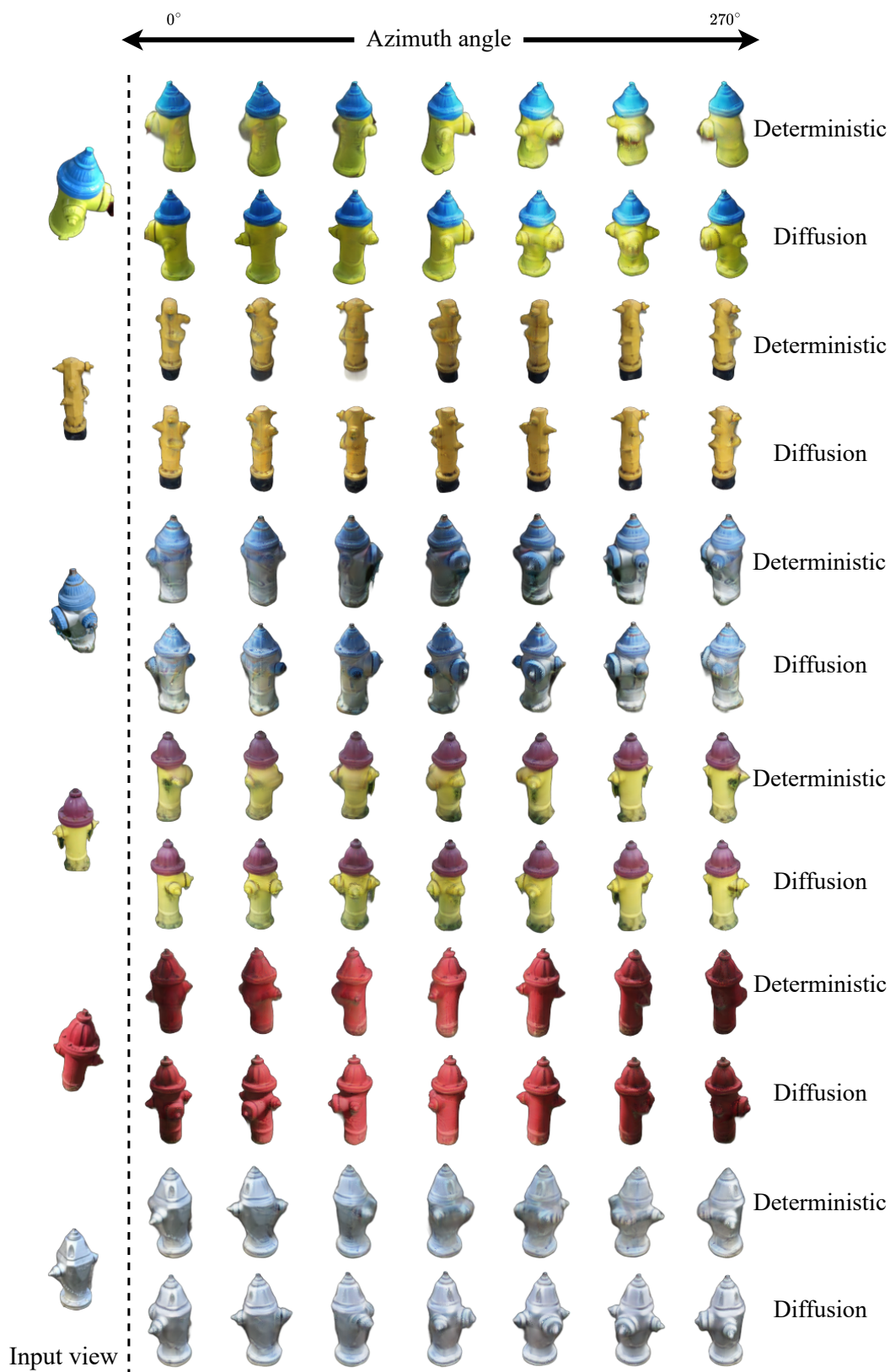


Figure 15: Qualitative results of Hydrant in CO3D dataset.

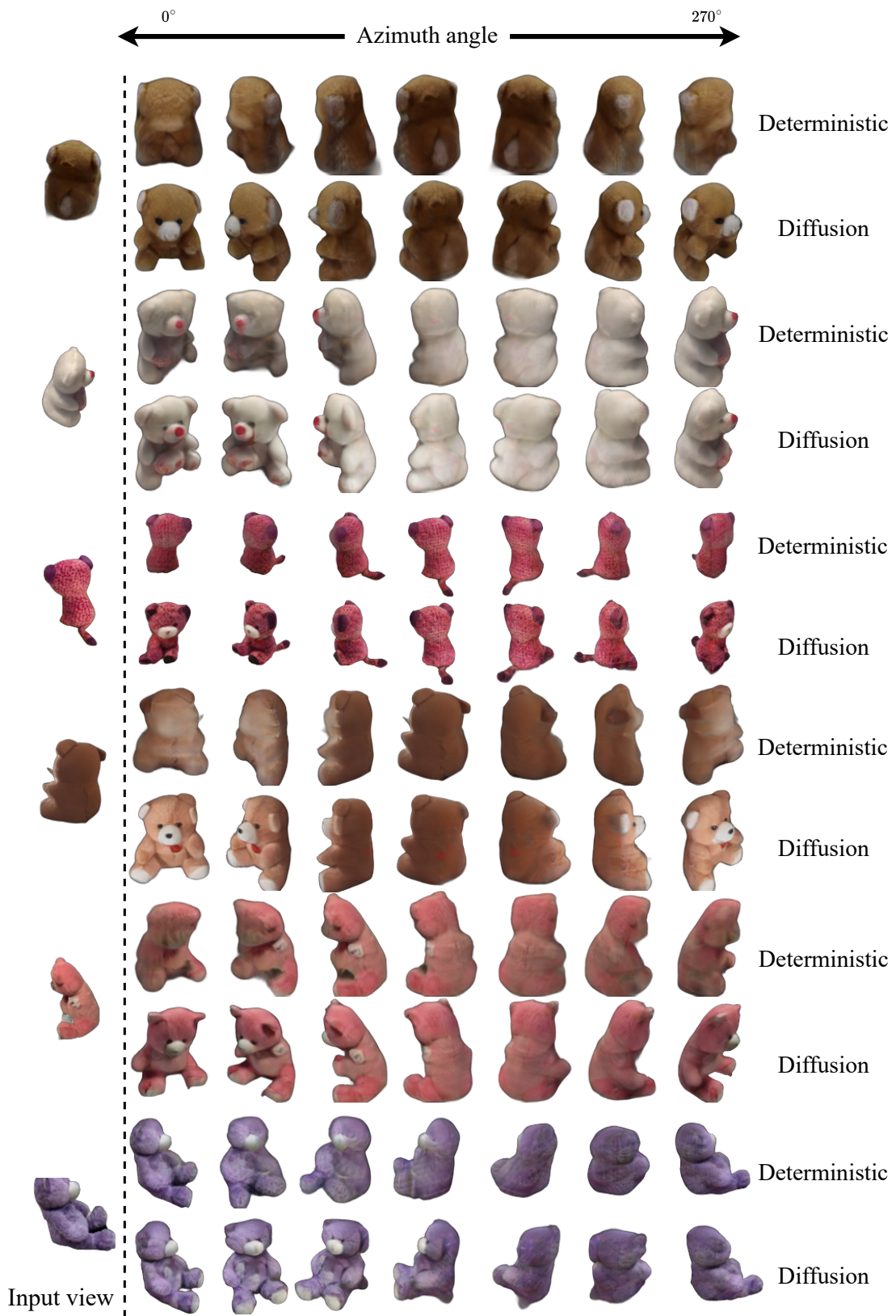


Figure 16: Qualitative results of Teddybear in CO3D dataset.

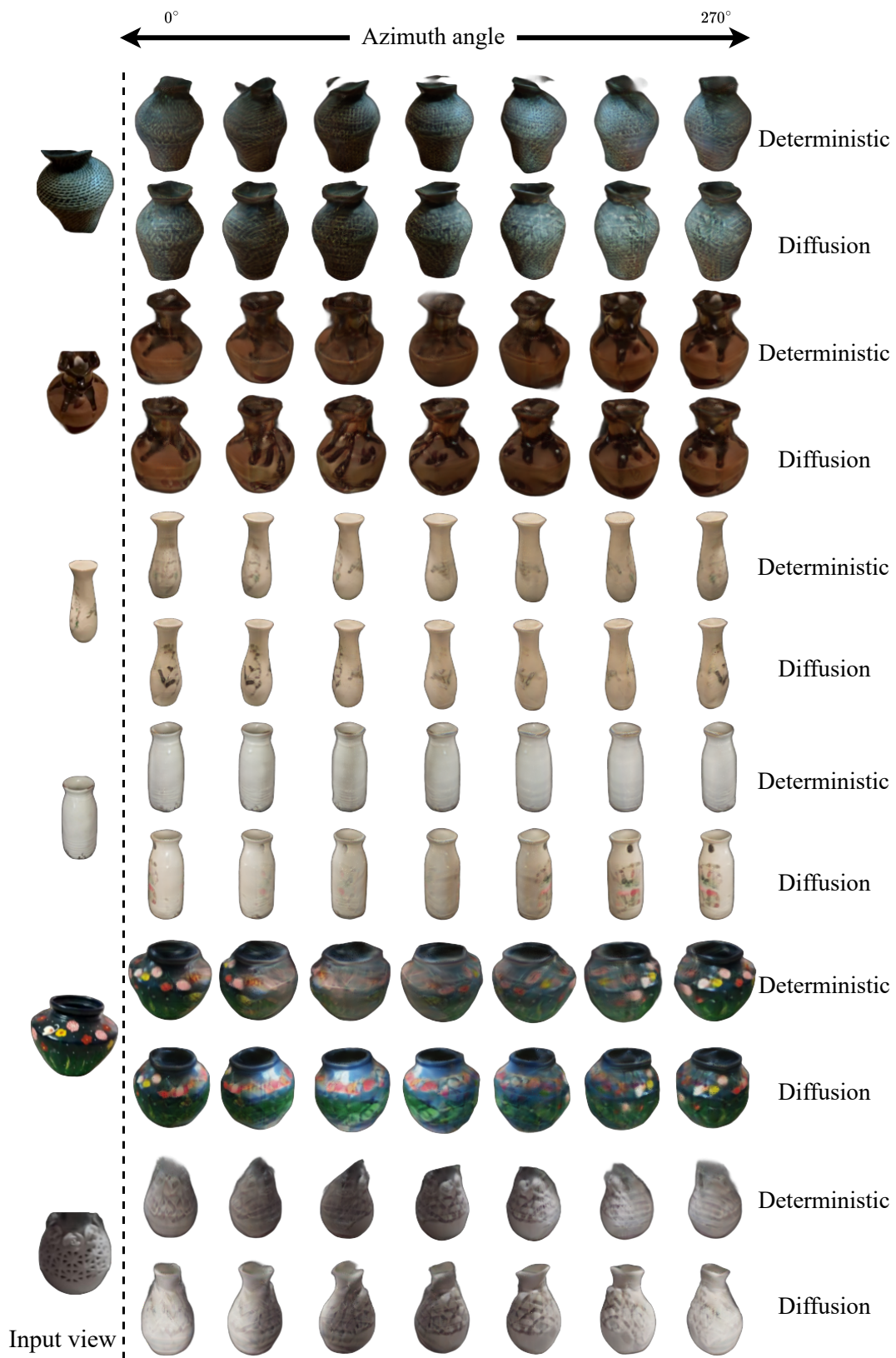


Figure 17: Qualitative results of Vase in CO3D dataset.

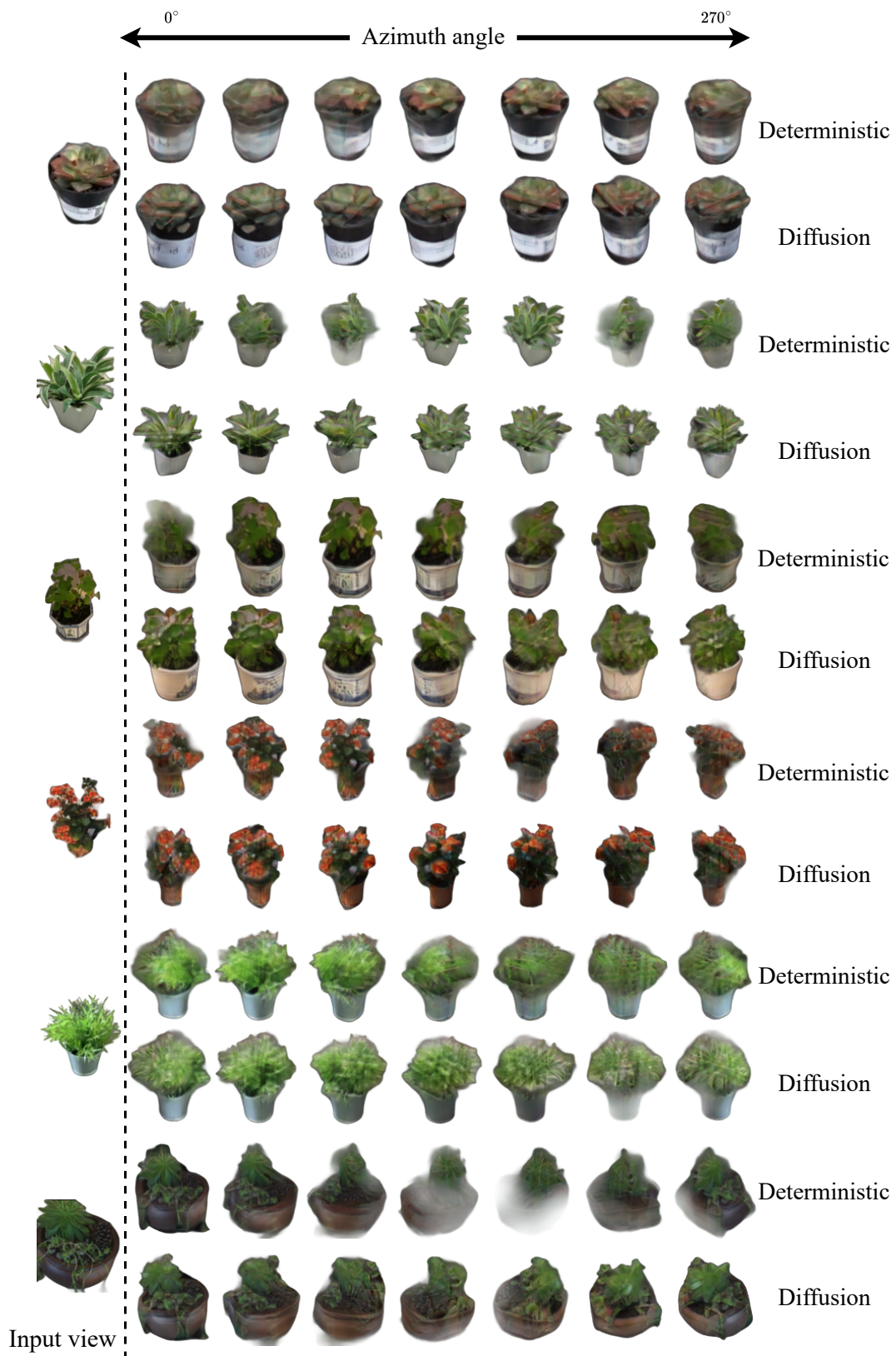


Figure 18: Qualitative results of Plant in CO3D dataset.

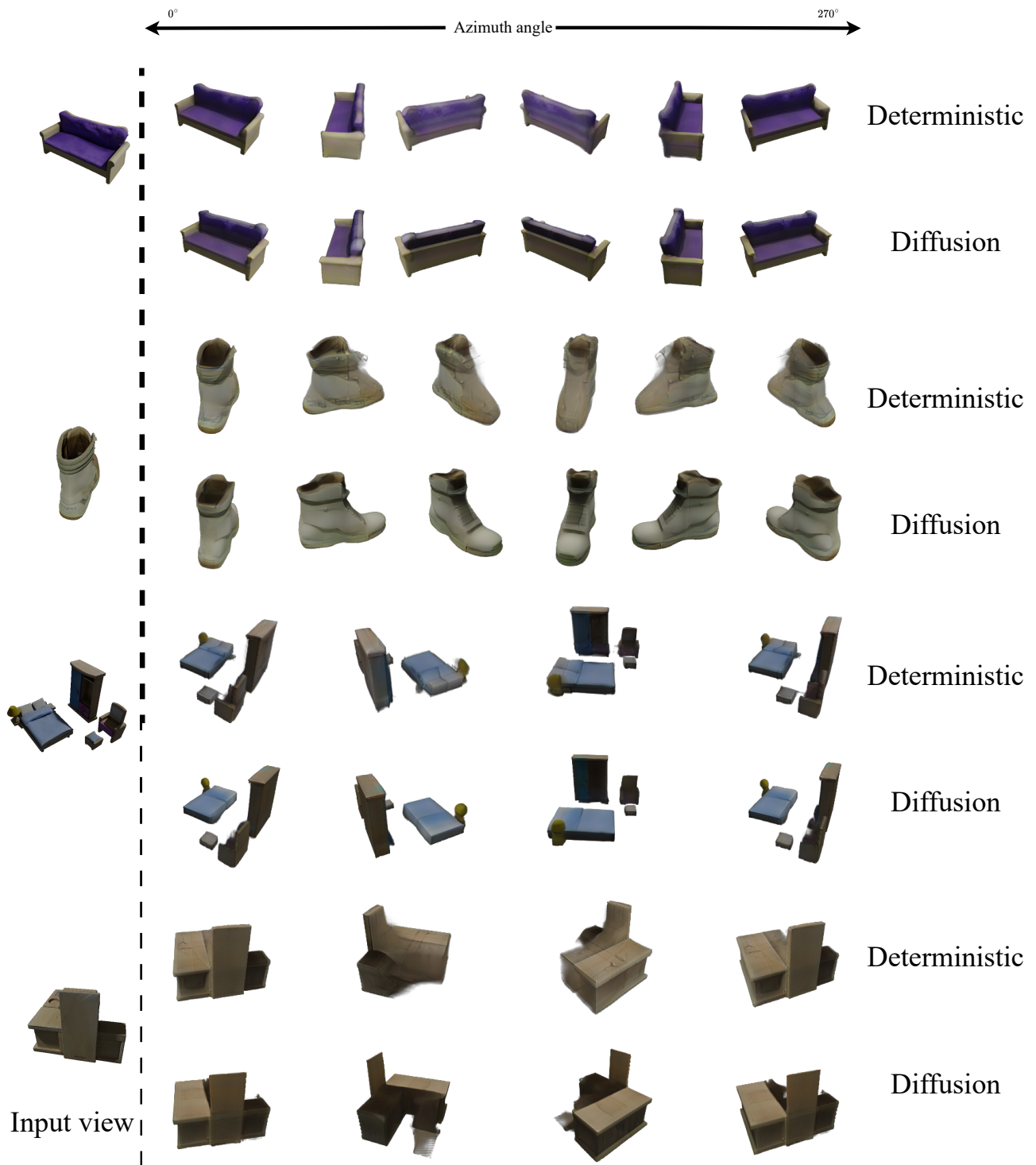


Figure 19: Single-view reconstruction results on GSO.

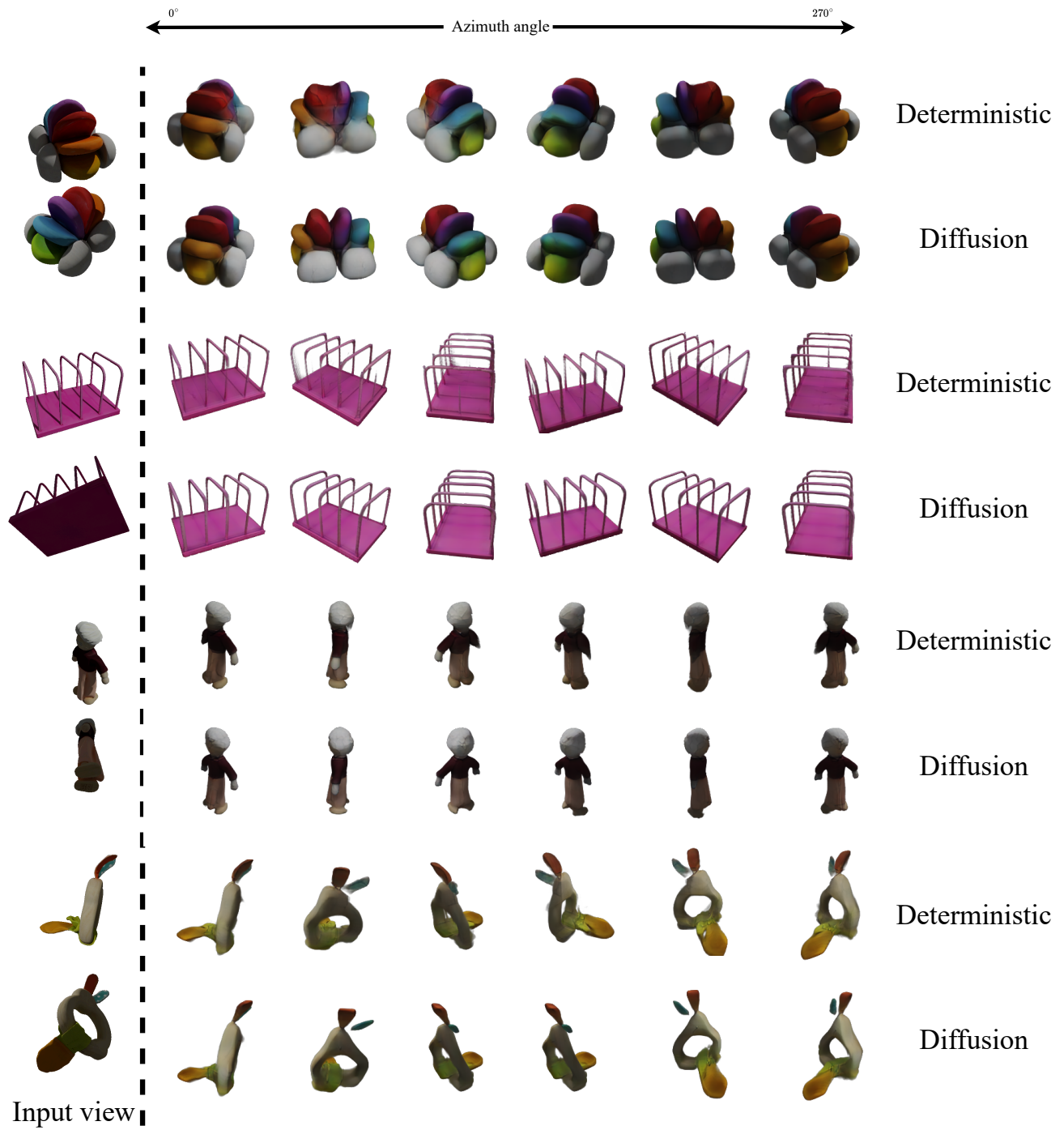


Figure 20: 2-views reconstruction results on GSO.

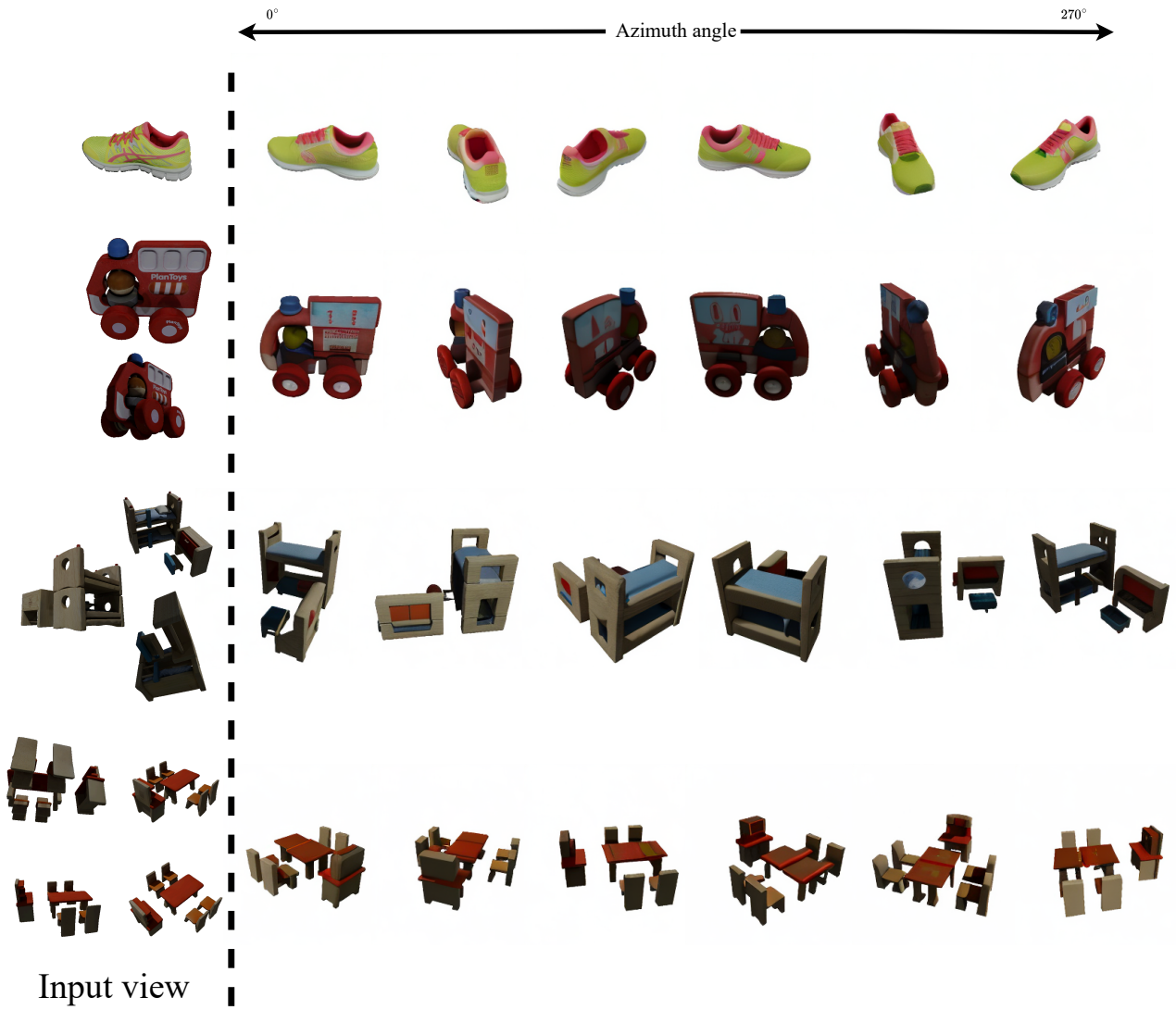


Figure 21: Sampling images from diffusion model on GSO.